

# Probing changes of dust properties along a chain of solar-type prestellar and protostellar cores in Taurus with NIKA\*

A. Bracco<sup>1</sup>, P. Palmeirim<sup>2,12</sup>, Ph. André<sup>1</sup>, R. Adam<sup>3,4</sup>, P. Ade<sup>6</sup>, A. Bacmann<sup>11</sup>, A. Beelen<sup>7</sup>, A. Benoît<sup>8</sup>, A. Bideaud<sup>8</sup>, N. Billot<sup>9</sup>, O. Bourrion<sup>3</sup>, M. Calvo<sup>8</sup>, A. Catalano<sup>3</sup>, G. Coiffard<sup>5</sup>, B. Comis<sup>3</sup>, A. D’Addabbo<sup>8,10</sup>, F.-X. Désert<sup>11</sup>, P. Didelon<sup>1</sup>, S. Doyle<sup>6</sup>, J. Goupy<sup>8</sup>, V. Könyves<sup>1</sup>, C. Kramer<sup>9</sup>, G. Lagache<sup>12</sup>, S. Leclercq<sup>5</sup>, J.F. Macías-Pérez<sup>3</sup>, A. Maury<sup>1</sup>, P. Maukopf<sup>6,13</sup>, F. Mayet<sup>3</sup>, A. Monfardini<sup>8</sup>, F. Motte<sup>11</sup>, F. Pajot<sup>7</sup>, E. Pascale<sup>6</sup>, N. Peretto<sup>6</sup>, L. Perotto<sup>3</sup>, G. Pisano<sup>6</sup>, N. Ponthieu<sup>11</sup>, V. Revéret<sup>1</sup>, A. Rigby<sup>6</sup>, A. Ritacco<sup>3,9</sup>, L. Rodriguez<sup>1</sup>, C. Romero<sup>5</sup>, A. Roy<sup>1</sup>, F. Ruppin<sup>3</sup>, K. Schuster<sup>5</sup>, A. Sievers<sup>9</sup>, S. Triqueneaux<sup>8</sup>, C. Tucker<sup>6</sup>, and R. Zylka<sup>5</sup>

<sup>1</sup> Laboratoire AIM, CEA/IRFU, CNRS/INSU, Université Paris Diderot, CEA-Saclay, 91191 Gif-Sur-Yvette, France  
e-mail: andrea.bracco@cea.fr

<sup>2</sup> Instituto de Astrofísica e Ciências do Espaço, Universidade do Porto, CAUP, Rua das Estrelas, PT4150-762 Porto, Portugal

<sup>3</sup> Laboratoire de Physique Subatomique et de Cosmologie, Université Grenoble Alpes, CNRS/IN2P3, 53, avenue des Martyrs, Grenoble, France

<sup>4</sup> Laboratoire Lagrange, Université Côte d’Azur, Observatoire de la Côte d’Azur, CNRS, Blvd de l’Observatoire, CS 34229, 06304 Nice cedex 4, France

<sup>5</sup> Institut de RadioAstronomie Millimétrique (IRAM), Grenoble, France

<sup>6</sup> Astronomy Instrumentation Group, University of Cardiff, UK

<sup>7</sup> Institut d’Astrophysique Spatiale (IAS), CNRS and Université Paris Sud, Orsay, France

<sup>8</sup> Institut Néel, CNRS and Université Grenoble Alpes, France

<sup>9</sup> Institut de RadioAstronomie Millimétrique (IRAM), Granada, Spain

<sup>10</sup> Dipartimento di Fisica, Sapienza Università di Roma, Piazzale Aldo Moro 5, I-00185 Roma, Italy

<sup>11</sup> Univ. Grenoble Alpes, CNRS, IPAG, F-38000 Grenoble, France

<sup>12</sup> Aix Marseille Université, CNRS, LAM (Laboratoire d’Astrophysique de Marseille) UMR 7326, 13388, Marseille, France

<sup>13</sup> School of Earth and Space Exploration and Department of Physics, Arizona State University, Tempe, AZ 85287

<sup>14</sup> Université de Toulouse, UPS-OMP, Institut de Recherche en Astrophysique et Planétologie (IRAP), Toulouse, France

<sup>15</sup> CNRS, IRAP, 9 Av. colonel Roche, BP 44346, F-31028 Toulouse cedex 4, France

<sup>16</sup> University College London, Department of Physics and Astronomy, Gower Street, London WC1E 6BT, UK

Accepted: 23 June 2017

## ABSTRACT

The characterization of dust properties in the interstellar medium (ISM) is key for understanding the physics and chemistry of star formation. Mass estimates are crucial to determine gravitational collapse conditions for the birth of new stellar objects in molecular clouds. However, most of these estimates rely on dust models that need further observational constraints to capture the relevant parameters variations depending on the local environment: from clouds to prestellar and protostellar cores.

We present results of a new study of dust emissivity changes based on millimeter (mm) continuum data obtained with the NIKA camera at the IRAM-30m telescope. Observing dust emission at 1.15 mm and 2 mm allows us to constrain the dust emissivity index,  $\beta$ , in the Rayleigh-Jeans tail of the dust spectral energy distribution (SED) far from its peak emission, where the contribution of other parameters (i.e. dust temperature) is more important. Focusing on the Taurus molecular cloud, one of the most famous low-mass star-forming regions in the Gould Belt, we analyze the emission properties of several distinct objects in the B213 filament. This sub-parsec size region is of particular interest since it is characterized by the presence of a collection of evolutionary stages of early star formation: three prestellar cores, two Class-0/I protostellar cores and one Class-II object. We are therefore able to compare dust properties among a sequence of sources that likely derive from the same parent filament.

By means of the ratio of the two NIKA channel-maps, we show that in the Rayleigh-Jeans approximation,  $\beta_{RJ}$  varies among the objects: it decreases from prestellar cores ( $\beta_{RJ} \sim 2$ ) to protostellar cores ( $\beta_{RJ} \sim 1$ ) and the Class-II object ( $\beta_{RJ} \sim 0$ ). For one prestellar and two protostellar cores, we produce a robust study using available *Herschel* data to constrain the dust temperature of the sources. By using the Abel transform inversion technique we get accurate radial temperature profiles that allow us to obtain radial  $\beta$  profiles. We find systematic spatial variations of  $\beta$  in the protostellar cores that is not observed in the prestellar core. While in the former case  $\beta$  decreases toward the center (with  $\beta$  varying between 1 and 2), in the latter it remains constant ( $\beta = 2.4 \pm 0.3$ ). Moreover, the dust emissivity index appears anticorrelated with the dust temperature. We discuss the implication of these results in terms of dust grain evolution between pre- and protostellar cores.

**Key words.** Interstellar Dust, Dust Emissivity, Protostars, Prestellar Cores, Molecular Clouds, ISM

\*Based on observations carried out under project number 146-13 with the IRAM 30m Telescope. IRAM is supported by INSU/CNRS (France), MPG (Germany) and IGN (Spain).

## 1. Introduction

The sub-millimeter (sub-mm) dust continuum images obtained with the *Herschel* space observatory unveiled the ubiquitous

filamentary structure of molecular clouds in the interstellar medium (ISM) (e.g. Men'shchikov et al. 2010; Molinari et al. 2010; Hill et al. 2011). Despite the open debate about the filament formation process in the magnetized and turbulent ISM, filaments are now conceived as crucial pieces of the puzzle of low-mass star formation (see André et al. 2014, for a review). *Herschel* data show that dense filaments are the preferred loci within molecular clouds where prestellar cores form and eventually evolve into protostars and pre-main sequence objects (e.g. André et al. 2010; Könyves et al. 2015). The progenitors of solar-type stars are believed to go through an evolutionary sequence that consists of five main stages (Lada 1987; André et al. 2000). When a self-gravitating prestellar core becomes gravitationally unstable the protostellar stage begins. Depending on the fraction of accreted mass from the protostellar envelope ( $M_{\text{env}}$ ) onto the central protostellar object ( $M_{\star}$ ), two protostar stages can be distinguished (Class-0,  $M_{\text{env}} > M_{\star}$ , and Class-I,  $M_{\text{env}} < M_{\star}$ , André et al. 1993), before most of the mass finally accumulates into the central pre-main sequence star, which also spawns a protoplanetary disk evolving into a debris disk (Class-II and Class-III, Greene et al. 1994). At some point along this evolutionary sequence, dust grains are expected to undergo a rapid growth, eventually leading to the formation of pebbles and planetesimals. Constraining the process of grain growth, which ultimately produces planet formation within protoplanetary disks, is the subject of active observational research (e.g. Testi et al. 2014).

In this context, two major issues in low-mass star formation studies are 1) likely evolution of dust properties from the diffuse ISM to dense cores to protoplanetary disks, and 2) accurate mass and column density estimates of star-forming structures. Many observational works tackling these issues rely on fitting the spectral energy distribution (SED) of thermal dust emission at far-infrared (FIR) and sub-mm wavelengths, where dust emission is usually optically thin (Hildebrand 1983) and therefore a good tracer of the total mass and column density (of dust and gas) integrated along the line of sight. The bulk of the interstellar dust mass is made of big dust grains (BG) in thermal equilibrium with the interstellar radiation field (ISRF). These grains emit as greybodies with an equilibrium temperature of few tens of Kelvin, depending on the local environment (Boulanger et al. 1996; Lagache et al. 1998). Given one BG population, its emission spectrum (in the optically thin regime) as a function of frequency is of the form

$$I_{\nu} = \tau_{\nu} B_{\nu}(T_{\text{d}}) = \kappa_{\nu} \Sigma B_{\nu}(T_{\text{d}}), \quad (1)$$

where  $I_{\nu}$  is the specific brightness (intensity),  $\tau_{\nu}$  is the frequency-dependent optical depth,  $B_{\nu}(T_{\text{d}})$  is the Planck function at the temperature  $T_{\text{d}}$  (the equilibrium temperature of the grains),  $\kappa_{\nu}$  is the dust opacity (in  $\text{cm}^2 \text{g}^{-1}$ ), and  $\Sigma$  is the gas surface density distribution. The latter can be written as  $\Sigma = \mu_{\text{H}_2} m_{\text{H}} N_{\text{H}_2}$ , given the mean molecular weight per hydrogen molecule  $\mu_{\text{H}_2}$ , the mass of the hydrogen atom  $m_{\text{H}}$ , and the column density of molecular hydrogen  $N_{\text{H}_2}$ . The dependence of  $\kappa_{\nu}$  on the frequency is usually expressed as

$$\kappa_{\nu} = \kappa_0 \left( \frac{\nu}{\nu_0} \right)^{\beta}, \quad (2)$$

where  $\kappa_0$  is the emissivity cross-section per gram of dust and gas at the frequency  $\nu_0$ , and  $\beta$  is the dust emissivity index. The shape of the observed SED mainly depends on  $T_{\text{d}}$  and  $\beta$ , while its offset level on  $\Sigma$ . The dust temperature controls the frequency position of the SED peak. It is set by the strength of the ISRF and by the emitting grain size distribution, since bigger grains have a

lower equilibrium temperature than smaller grains (Mathis et al. 1977; Weingartner & Draine 2001). Less obvious is the dependence of  $\beta$  on dust properties (Draine 2006). It relates to the dust structure and composition, which determine both the optical/UV absorption cross-section and the emission cross-section of the grains, and the frequency-dependent efficiency to emit radiation (see Eq. (2)) (Compiègne et al. 2011; Jones et al. 2017). It follows that the mass estimate of a *dusty* source depends on all possible assumptions related to these parameters.

Several works at FIR and sub-mm wavelengths studied how properties of dust emission vary, both at large scales in the more diffuse ISM (Bracco et al. 2011; Planck Collaboration XI 2014; Ysard et al. 2015) and at small scales in star-forming regions (Stepnik et al. 2003; Paradis et al. 2010; Ysard et al. 2013; Sadavoy et al. 2013; Roy et al. 2014). However, disentangling the contributions of  $\beta$  and  $T_{\text{d}}$  variations in dust SEDs is a difficult task in the FIR and sub-mm domains. One of the keys to this problem is to probe dust emission at longer wavelengths in the Rayleigh-Jeans portion of the SED, where temperature effects are less important. Thus, the millimeter (mm) range is crucial to investigate dust emissivity index variations. While some models still assume  $\beta$  to be constant (equal to 2 for crystalline dust grains, Draine & Li (2007); Compiègne et al. (2011)), recent observational results between 1 and 3 mm (i.e., Schnee et al. 2014; Sadavoy et al. 2016) revealed  $\beta$  variations in the Orion molecular cloud, which may be caused by possible dust evolution in protostars. Changes of  $\beta$  at smaller scales in protoplanetary disks were also observed and interpreted as consequence of dust grain-growth in disk formation (Draine 2006; Guilloteau et al. 2011).

In this paper we present new results from millimeter continuum observations of a portion of the Taurus molecular cloud, obtained in winter 2014 with the Institut de Radio Astronomie Millimétrique (IRAM) 30-m telescope using the dual-band capability of the New IRAM KID Arrays (NIKA, Monfardini et al. 2011; Calvo et al. 2013; Adam et al. 2014; Catalano et al. 2014). This prototype instrument enabled us to simultaneously map at  $\sim 1.15$  mm (band-1) and  $\sim 2$  (band-2) mm a  $8' \times 5'$  segment of the B213 filament in the Taurus molecular cloud, where three prestellar cores, two Class-0/I protostellar cores and one Class-II object are embedded. We propose an original analysis of dust-emissivity-index spatial variations associated with several evolutionary stages of early star formation for objects that likely originated from the same parent filament.

In this work we make use of both NIKA and *Herschel* data, which we combine avoiding biases due to the different data acquisition process of the two instruments. We base our analysis on the ratio map between the two NIKA channels. Putting constraints on the dust temperature of the observed sources by means of the *Herschel* data only, we are able to infer radial changes of  $\beta$  that correlate with the presence of protostars.

This study highlights the capabilities of the NIKA camera, which will be the starting point for a new observational campaign in star forming regions with the advent of the NIKA2 instrument in both intensity and polarization (Calvo et al. 2016).

The paper is organized as follows. Section 2 describes the B213 filament in the Taurus molecular cloud and the main sources we focus on. In Sect. 3 we present NIKA and the data reduction process. Section 4 introduces the ratio map between the two NIKA bands, which guides our data analysis. The study of the dust-emissivity variations among the various targets inferred from the ratio map is presented in Sect. 5, while the discussion of the results is in Sect. 6. We conclude this paper with summary and prospects in Sect. 7.

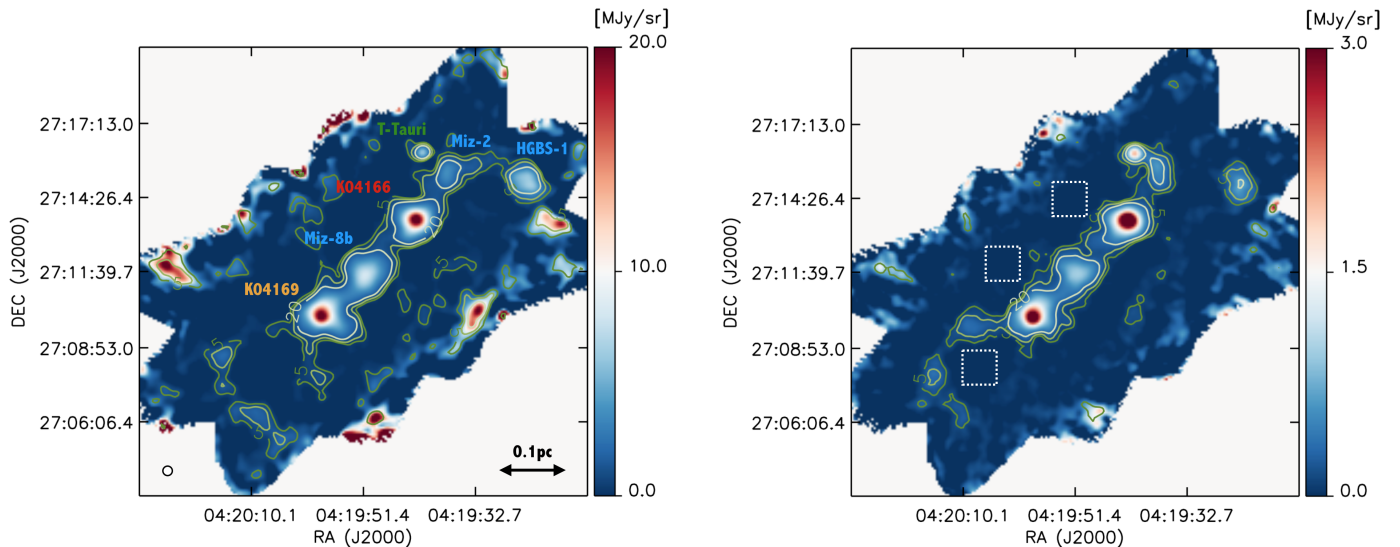


**Fig. 1.** Dust continuum maps of a portion of the B213 filament obtained with the NIKA camera on the IRAM 30 m telescope at 1.15 mm (left panel) and 2 mm (right panel). The two maps are shown after smoothing to a common resolution of  $24''$  (see the circle on the left-bottom part of the left panel). The green contours represent the signal-to-noise levels (5, 10, 20) at each wavelength. The labels in the left panel correspond to the sources analyzed in this work and described in Table 1. The three squares on the right delimit the regions where we estimate the rms intensity of the two maps at  $24''$ , which corresponds to 0.75 MJy/sr and 0.09 MJy/sr at 1.15 mm and 2 mm respectively.

Object	Evolutionary Stage	RA (J2000)	DEC (J2000)	Abbreviation in text and figures
HGBS-J041937.7+271526 <sup>a,c</sup>	Prestellar	04h 19m 37.7s	+27° 15' 20.0"	Miz-2
HGBS-J041923.9+271453 <sup>e</sup>	Prestellar	04h 19m 23.9s	+27° 14' 53.0"	HGBS-1
Miz-8b <sup>a,c</sup>	Prestellar	04h 19m 51.0s	+27° 11' 42.2"	Miz-8b
K04166 <sup>b</sup>	Class-0/I	04h 19m 42.9s	+27° 13' 38.8"	K04166
K04169 <sup>b</sup>	Class-0/I	04h 19m 58.9s	+27° 10' 00.5"	K04169
J04194148+2716070 <sup>d</sup>	T-Tauri	04h 19m 41.5s	+27° 16' 07.0"	T-Tauri

**Table 1.** Description of the analyzed prestellar and protostellar objects in the B213 filament (a,b,c,d,e - Mizuno et al. 1994; Motte & André 2001; Tatematsu et al. 2004; Davis et al. 2010; Marsh et al. 2016, respectively). Celestial coordinates are given according to the corresponding positions in the NIKA maps.

## 2. B213 filament and its embedded objects

The Taurus molecular cloud is one of the closest ( $d \sim 140$  pc, Elias (1978)) and well studied low-mass star-forming region in the Gould Belt. Most of its young stars are grouped in elongated patterns that are closely associated with a network of prominent parallel filaments (e.g. Schneider & Elmegreen 1979; Hartmann 2002). B213 is one of the most dominant filaments that is actively forming stars (Schmalzl et al. 2010; Li & Goldsmith 2012), where several embedded prestellar and protostellar cores are clearly detected along its crest (Onishi et al. 2002; Marsh et al. 2016).

*Herschel* Gould Belt Survey (HGBS) observations revealed the density and dust temperature structure of B213 with unprecedented detail. Palmeirim et al. (2013) argued that the filament is self-gravitating and currently contracting quasi-statically toward its longest axis while accreting material from the surrounding environment. Its radial density profile approaches power-law behavior,  $\rho \propto r^{-2}$  at large radii, and the temperature profile significantly drops toward the crest. They report central average values

for the dust temperature and gas volume density in the filament of 11.8 K and  $\sim 5 \times 10^4$  cm<sup>-3</sup>, respectively.

In the NIKA maps of the segment of B213 displayed in Fig. 1 we can see six bright sources, which are listed in Table 1. Three of them are prestellar cores (hereafter, Miz-8b, Miz-2, HGBS-1 (see Mizuno et al. 1994; Marsh et al. 2016) in blue in Fig. 1). Miz-8b is also detected in  $N_2H^+(1-0)$  observations with the Nobeyama 45 m telescope (Tatematsu et al. 2004). The other three sources are not prestellar cores but bright point-like objects detected by *Herschel* PACS at  $70\mu\text{m}$ . Two of them, those neighbouring Miz-8b, are protostellar cores classified as Class-0/I objects (hereafter, K04166 and K04169<sup>1</sup> (Motte & André 2001; Tafalla et al. 2010)), which are known to drive bipolar outflows (Bontemps et al. 1996; Tafalla et al. 2004; Santiago-García et al. 2009). As shown in Fig. 5 of Motte & André (2001) by the envelope-mass versus bolometric-luminosity plot, the two sources are border-line Class-0/Class-I

<sup>1</sup> The first letter  $\hat{\text{A}}\hat{\text{I}}\hat{\text{J}}\hat{\text{K}}\hat{\text{A}}\hat{\text{I}}$  of the adopted names recalls IRAS sources selected by Kenyon et al. (1990, 1993).

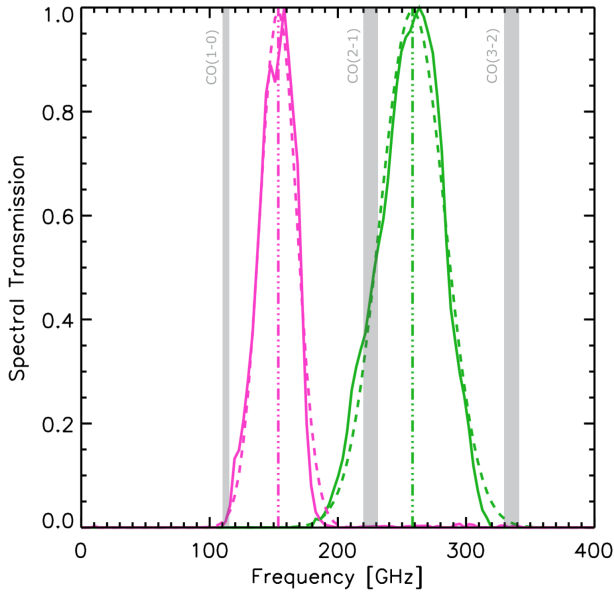


**Fig. 2.** Spectral transmission of the two NIKA bands. The dashed curves represent Gaussian fits to the bandpasses. The central peaks, marked with vertical-dotted lines, are at  $(260 \pm 25)$  GHz ( $\sim 1.15$  mm) in green and  $(150 \pm 14)$  GHz ( $\sim 2$  mm) in pink. The grey shades show the CO transitions that fall into the NIKA bandpasses.

objects with strong near-infrared emission (Kenyon et al. 1993; Furlan et al. 2008).

In the north-western direction of the field of view a more evolved object (J04194148+2716070) classified as a Class-II T-Tauri star can be also seen (Davis et al. 2010).

In-depth analysis of molecular line observations of this field have revealed the presence of velocity coherent structures, referred to as “fibers” (Hacar et al. 2013), which overlap on the plane of the sky towards B213, with typical lengths of  $\sim 0.5$  pc. However, we note that the portion of B213 observed with NIKA corresponds to a single fiber. Thus, the objects discussed in this paper likely belong to the same parent physical structure. The fact that these objects are different evolutionary stages of early star formation evolved from the same structure, makes them an interesting case to study how the dust emissivity index varies as star formation proceeds.

### 3. Observations and data reduction

We made use of the dual-band capability of NIKA, which was used to observe part of B213 in the Taurus molecular cloud. The transmission curves of the two bands are displayed in Fig. 2. The central frequencies are  $260 \pm 25$  GHz (or  $\sim 1.15$  mm) for band-1 (with  $\sim 190$  valid pixels) and  $150 \pm 14$  GHz (or  $\sim 2$  mm) for band-2 (with  $\sim 125$  valid pixels). The two NIKA brightness maps,  $I_{1\text{mm}}$  and  $I_{2\text{mm}}$ , are shown in Fig. 1 in units of MJy/sr. Observations were performed during the first NIKA open pool, in February 2014. The observing conditions were stable with a mean zenith opacity of 0.13 in band-1 and 0.09 in band-2. Uranus was used as primary calibrator.

Given the broad coverage of the NIKA bandpasses (see Fig. 2), we applied average color corrections of 0.97 and 0.91 to the data in band-1 and band-2, respectively. These corrections were estimated integrating over the NIKA bandpasses greybodies for dust emission with spectral indices,  $\beta$ , varying between 1

and 3 and including the IRAM-30m atmospheric models for the mean opacities referred to above.

The overall calibration uncertainty, including the calibrator model uncertainty, was estimated to be 7% in band-2 and 12% in band-1 (Adam et al. 2015). Pointing corrections were checked using nearby quasars every hour, leading to a pointing rms accuracy better than  $3''$ . The telescope focus was checked about every 3 hours. The effective beam FWHM was measured to be  $18.2''$  and  $12.0''$  in band-2 and band-1, respectively. However, since in this work we also make use of *Herschel* data between  $160\mu\text{m}$  and  $350\mu\text{m}$  of B213 (see Sect. 5.2), the NIKA maps were smoothed to the resolution of  $24''$  (with  $5''$  pixels) of SPIRE- $350\mu\text{m}$ , assuming Gaussian beams for both NIKA channels. The error due to the Gaussian assumption of the smoothing kernel was found to be negligible compared to considering the actual NIKA point spread function of the two bands, and did not affect the results of the paper. The rms noise level at  $24''$  resolution was estimated on the three source-free square regions in the right panel of Fig. 1. It corresponds to  $0.75$  MJy/sr in band-1 and  $0.09$  MJy/sr in band-2<sup>2</sup>.

The signal was mapped using scans made of a set of sub-scans, separated by  $20''$  from each other, oriented perpendicular, and oriented with an angle of  $\pm 45^\circ$  with respect to the main filament axis. The scans cover a quasi homogeneous region of  $8' \times 5'$ . Such scanning strategy allows us to limit residual striping in the reduced maps, thanks to the variety in the scanning angles, and to limit filtering effects by allowing to define the surface brightness zero level in the external regions of the filament. The data in the two bands were reduced simultaneously and independently as described in Adam et al. (2015). In brief, the correlated noise (atmospheric and electronic) was removed by averaging and subtracting the detector timelines across the arrays. A small fraction of the scans were flagged due to bad weather conditions and some others were lost because of missing data streams with the telescope position. The overall effective time spent on target was 16.1 hours.

The data processing filtered out the astrophysical signal on scales larger than the NIKA field of view ( $\sim 2$  arcmin). The filtering was the same at both wavelengths (Adam et al. 2017), but the effective zero level brightness in each map was unconstrained. It was defined during the mapmaking procedure, in an iterative manner, by setting to zero the mean of the detector timelines in the low surface brightness parts of the filament, i.e., where the signal-to-noise ratio in the maps at their nominal resolutions was lower than 3. In order to take into account the uncertainty introduced by the mapmaking procedure, we tested the robustness of our results against four versions of the maps produced with different filtering criteria depending on the size of the mask used to define the background signal.

### 4. Ratio map between the two NIKA bands

To put constraints on the dust emissivity index variations in the mm-domain we study the ratio between the NIKA surface brightnesses. In Fig. 3 we show the ratio map,  $R_{1,2} = \frac{I_{1\text{mm}}}{I_{2\text{mm}}}$ , where we masked all pixels with a signal-to-noise ratio lower than 10 in at least one of the two bands at the resolution of  $24''$ . In the image it is possible to appreciate the difference in the value of  $R_{1,2}$  between the various objects. In particular, prestellar cores clearly exhibit a larger value of  $R_{1,2}$  compared to the other sources. The

<sup>2</sup>At the original NIKA resolution the rms noise level is 4 mJy/beam and 1 mJy/beam at 1.15 mm ( $12''$  beam) and at 2 mm ( $18.2''$  beam), respectively.



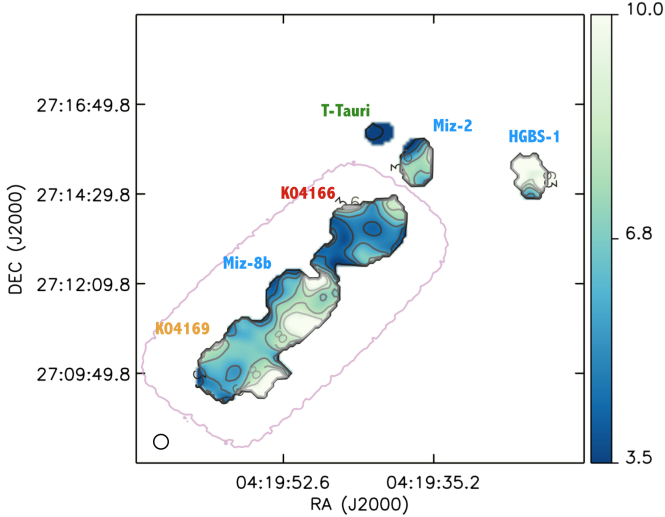


**Fig. 3.** Ratio map between the two NIKA bands,  $R_{1,2} = \frac{I_{1\text{mm}}}{I_{2\text{mm}}}$ . The unmasked region corresponds to a signal-to-noise ratio on the fluxes above 10 at both wavelengths. Black contours represent  $R_{1,2}$  equal to 3, 4.5, 5.6, 7, 8, and 9. The purple contour corresponds to the part of the field with homogeneous observing time  $> 240$  s per pixel (see Fig. A.1). The open circle at the bottom left represents the beam size ( $24''$ ).

lowest value of  $R_{1,2}$  corresponds to the position of the Class-II T-Tauri object, the most evolved object in the sample. In order to strengthen the change in  $R_{1,2}$  with evolutionary stage, the left panel of Fig. 4 presents four normalized histograms of  $R_{1,2}$ , where only the unmasked pixels in the maps are considered. The histogram corresponding to all unmasked pixels is shown in black. It peaks at  $\sim 7$  with a broad distribution skewed toward lower values. In colours we show the normalized histograms of  $R_{1,2}$  within one-beam area ( $24''$ ) centered around K04166 (red), K04169 (yellow), and Miz-8b (blue). For the remaining three objects we only display, with dashed-vertical lines, the value of  $R_{1,2}$  at the peak intensity positions of the T-Tauri star (green) and the prestellar cores Miz-2 and HGBS-1 (blue). As detailed in Appendix A, the observing time was not completely homogeneous across the NIKA maps (see Fig. A.1). For this reason our study mainly focuses on the sources with the longest observing time, corresponding to K04166, K04169, and Miz-8b (see the purple contour in Fig. 3). Nevertheless Fig. 4 also shows the peak  $R_{1,2}$  values measured for the other objects. The difference among all sources is striking. While prestellar cores present values of  $R_{1,2}$  of  $\sim 8$ , the ratio progressively decreases to  $\sim 5.5$  and  $\sim 4.3$  for the protostellar cores and to  $\sim 3$  for the Class-II T-Tauri object.

These variations of  $R_{1,2}$  in the wavelength regime probed by NIKA are difficult to explain without invoking changes in the dust emissivity index of the sources. In the right panel of Fig. 4 the result of a simple exercise to test this assessment is shown. Assuming a greybody spectrum for dust emission (see Eq. 1), we verify the effect on  $R_{1,2}$  of significant variations of  $T_d$  but negligible changes in  $\beta$ , and vice-versa. Thus, on top of the normalized histogram of  $R_{1,2}$ , we display with green shades the range of values that we would get with  $10\text{K} < T_d < 20\text{K}$  for a fixed  $\beta = 2$ , and with purple shades the range of  $R_{1,2}$  for a fixed  $T_d = 15\text{K}$  and  $0.5 < \beta < 3$ . The specific values of the parameters are not critical for this test. The figure clearly shows the impact of vary-

ing  $\beta$  in this wavelength range compared to changes in  $T_d$ . The range of  $R_{1,2}$  expected from plausible  $\beta$  variations allows us to recover almost 95% of the values observed with NIKA in Fig. 3.

## 5. Variations of the dust emissivity index from the ratio map

In the following section we derive the dust emissivity index,  $\beta$ , for K04166, K04169, and Miz-8b from the ratio map,  $R_{1,2}$ , introduced in Sect. 4. We first estimate  $\beta$  in the Rayleigh-Jeans limit and then produce a more accurate evaluation using constraints on the dust temperature of the sources based only on *Herschel* data.

### 5.1. $\beta$ values in the Rayleigh-Jeans limit

In the previous section we showed how variations of  $\beta$  can affect dust emission at long wavelengths compared to changes in  $T_d$ . This suggests that we can, to first order, consider the Rayleigh-Jeans limit of the Planck function ( $h\nu \ll k_B T_d$ , where  $h$  and  $k_B$  are the Planck's and the Boltzmann's constants, respectively<sup>3</sup>) to directly deduce the values of  $\beta$  from  $R_{1,2}$ . Under this assumption we write  $B_\nu(T_d) \approx 2k_B T_d \nu^2 c^{-2}$ , so that, from Eq. 1 and Eq. 2,  $\beta$  as a function of  $R_{1,2}$  is

$$\beta_{\text{RJ}} = \frac{\log R_{1,2}}{\log(\nu_{1\text{mm}}/\nu_{2\text{mm}})} - 2, \quad (3)$$

where  $\nu_{1\text{mm}}$  and  $\nu_{2\text{mm}}$  are  $\sim 260$  GHz and  $\sim 150$  GHz respectively and the subscript ‘‘RJ’’ stands for Rayleigh-Jeans.

The top x-axis of the left panel of Fig. 4 shows an indicative scale with the corresponding values of  $\beta_{\text{RJ}}$ . The overall distribution peaks at  $\beta_{\text{RJ}} = 1.4$  and ranges from very low values below  $\beta_{\text{RJ}} \sim 0.5$  to large values above  $\beta_{\text{RJ}} \sim 3$ . As for  $R_{1,2}$ , we find a clear difference between the  $\beta_{\text{RJ}}$  values for protostellar cores (0.6, 1.1) and for prestellar cores ( $\sim 2$ ). Clearly, protostellar cores tend to have lower values of  $\beta_{\text{RJ}}$  compared to prestellar cores.

We notice that the lowest values of  $\beta_{\text{RJ}} \sim 0$  mostly relate to the Class-II object, which may be enough optically thick to justify these low values. However a more detailed and accurate discussion is not possible since the Class-II object is located in the part of the maps with varying sensitivity and observing time (see Appendix A).

### 5.2. Radial profiles: from *Herschel* dust temperatures to $\beta$

In order to go beyond the simple Rayleigh-Jeans approximation we produce a more detailed analysis, which relies on putting constraints on the dust temperature structure of each source using *HGBS* data for B213 (Palmeirim et al. 2013; Marsh et al. 2016). For this detailed analysis, we only consider K04166, K04169, and Miz-8b, which are the three objects observed with the most homogeneous sensitivity with NIKA (cf. Fig. A.1 and purple contour in Fig. 3).

The *Herschel* data allow us to estimate the dust temperature of each source since the PACS and SPIRE maps probe the peak of the dust SED between  $160\ \mu\text{m}$  and  $500\ \mu\text{m}$ .

Our framework is the following: we use *Herschel* data at wavelengths close to the peak of the dust SED to best evaluate  $T_d$ ; we make use of NIKA data at mm-wavelengths in the Rayleigh-Jeans portion of the SED to estimate  $\beta$ .

<sup>3</sup> At 260 GHz the Rayleigh-Jeans limit corresponds to  $T_d \gg 12\text{K}$

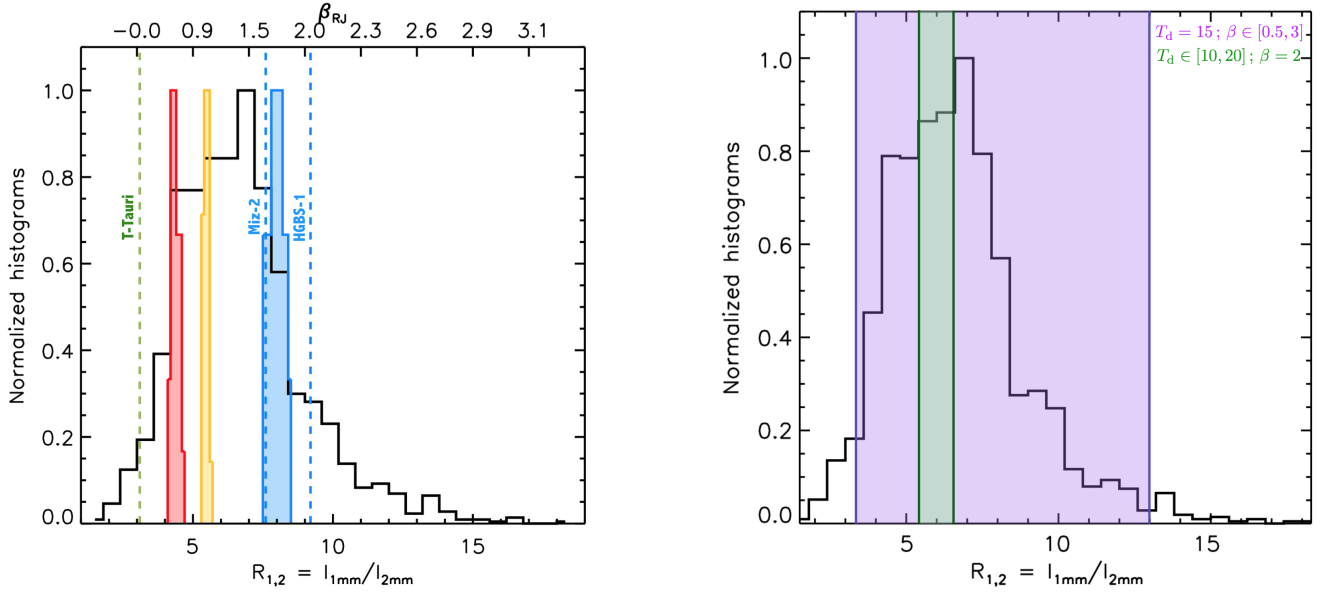


**Fig. 4.** *Left:* normalized histogram of  $R_{1,2}$  in black for all the unmasked pixels in the maps. The coloured normalized histograms represent the  $R_{1,2}$  distributions within one-beam area ( $24''$ ) around the central coordinates (see Table 1) of K04166 (red), K04169 (yellow), and Miz-8b (blue). The vertical dashed lines refer to the value of the ratio at the peak-intensity position of T-Tauri (green), Miz-2, and HGBS-1 (blue). The upper x-axis shows the corresponding  $\beta$  values in the Rayleigh-Jeans limit (see Sect. 5.1). *Right:* same as in the left panel with shades that now represent ranges of  $R_{1,2}$  corresponding to greybodies with 1) a constant temperature  $T_d$  of 15 K but a varying  $\beta$  between 0.5 and 3 in purple; 2) a constant  $\beta$  of 2 but varying  $T_d$  between 10 K and 20 K in green.

An accurate estimate of the temperature for compact sources, such as those presented in this study, requires some caution. A single-temperature greybody fit of the dust SED (see Eq. 1) provides us with a value of the temperature of a given source averaged along the line of sight. This approach neglects possible temperature gradients within the observed objects caused by internal (protostellar case) or external (prestellar case) radiation fields. Because of this effect, the mass estimate of the sources may be also affected (e.g. Malinen et al. 2011; Roy et al. 2014).

Thus, to estimate the dust temperature profiles of our three sources we make use of the reconstruction method described in Roy et al. (2014), which consists in an inversion technique based on the Abel integral transform applied to the *Herschel* data between PACS-160  $\mu\text{m}$  and SPIRE-350  $\mu\text{m}$ .

Under the assumption of spherical symmetry for a source embedded in a uniform radiation field and with radial density profile  $\rho(r)$ , the specific intensity  $I_\nu(p)$  observed at a distance  $p$  from the center of the source can be expressed as

$$I_\nu(p) \cong 2 \int_p^{+\infty} \rho(r) B_\nu(T_d(r)) \kappa_\nu \frac{r dr}{\sqrt{r^2 - p^2}}. \quad (4)$$

The Abel transform allows us to infer the integrand of the above equation given the intensity at each frequency as

$$\rho(r) B_\nu(T_d(r)) \kappa_\nu = -\frac{1}{\pi} \int_r^{+\infty} \frac{dI_\nu}{dp} \frac{dp}{\sqrt{p^2 - r^2}}. \quad (5)$$

Assuming spherical symmetry, the derivatives of the radial intensity profiles are sufficient to estimate  $\rho(r)$  and  $T_d(r)$ . Given  $\kappa_\nu$  we can simultaneously obtain the density (or column density,  $N_{\text{H}_2}$ , if the line-of-sight integration is considered) and temperature radial profiles by fitting a single temperature greybody to the *Herschel* SED between 160  $\mu\text{m}$  and 350  $\mu\text{m}$ . We ignore here SPIRE-500  $\mu\text{m}$  since we want to get advantage of the highest

possible resolution of the NIKA dual-band data. In this case the greybody fit of the *Herschel* data is performed with  $\beta = 2$  and, from Roy et al. (2014),

$$\kappa_\nu = 0.1 \times (\lambda/300 \mu\text{m})^{-2} \text{ cm}^2/\text{g}. \quad (6)$$

Nevertheless, we produce temperature radial profiles considering both  $\beta = 2$  and  $\beta = 1.55$ , with no significant impact on the results. We notice that thanks to the SED frequency coverage provided by the HGBS data no degeneracy exists between density and temperature through the Abel reconstruction. While the shape of the SED is constrained by the dust temperature, the strength of the sub-mm continuum emission is set by the density. In the left panel of Fig. 5 we show the radial profiles of  $T_d$  with the usual color code corresponding to the three sources under study. The data points are the Abel-reconstructed temperatures while, for comparison, the dashed lines show the line-of-sight SED dust temperatures. As expected, the main difference between the two cases is at the center of the sources, where the line-of-sight temperature underestimates the true value of  $T_d$  for the protostellar objects and overestimates it for the prestellar core. On the other hand, the Abel-reconstructed and the line-of-sight dust temperatures tend to agree at large radii from source center.

Given these radial temperature profiles, we can now go beyond the Rayleigh-Jeans approximation presented in Sect. 5.1 and use  $T_d(r)$  to perform a more rigorous estimate of  $\beta$  at radius,  $r$ , from the center of each source, as follows

$$\beta(r) = \frac{\log \{R_{1,2} \times B_{\nu_{2\text{mm}}}[T_d(r)] / B_{\nu_{1\text{mm}}}[T_d(r)]\}}{\log(\nu_{1\text{mm}}/\nu_{2\text{mm}})}. \quad (7)$$

In the right panel of Fig. 5 we display the radial profiles of  $\beta$  with the same colour code as in the left panel. The error bars represent the combination of the  $1 \sigma$  uncertainties derived from

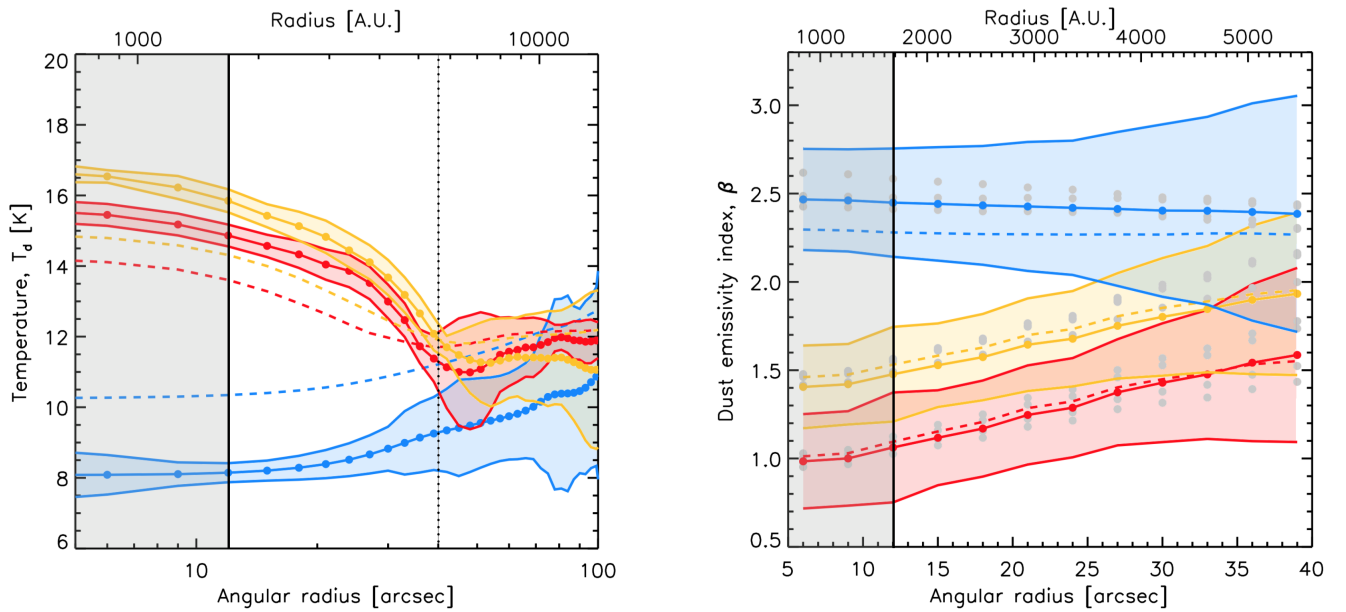


**Fig. 5.** *Left:* Dust temperature radial profiles of K04166 (red), K04169 (yellow), and Miz-8b (blue). The dust temperatures were derived from *Herschel* Gould Belt survey data (<http://gouldbelt-herschel.cea.fr/archives/>). The dashed-coloured lines correspond to line-of-sight averaged temperatures obtained from direct SED fitting, while the dots and the solid lines correspond to Abel-reconstructed dust temperatures. The coloured shades represent the  $1\text{-}\sigma$  errors of the Abel-reconstructed temperatures. *Right:* radial profiles of  $\beta$  using the Abel-reconstructed temperatures. The colour-code is the same as in the left panel. The grey dots show the  $\beta$  profiles corresponding to four different versions of the maps used to quantify systematic effects due to spatial filtering in the data. The grey-shaded area in both panels indicates radial distances below the half-beam width of  $12''$ . The Abel transform is only performed for radial distances smaller than the dotted-black vertical line in the left panel. On the upper x-axis the radial distance is in astronomical units assuming a distance of 140pc for the Taurus molecular cloud.

propagating the statistical errors in<sup>4</sup>  $R_{1,2}$  and  $T_d$  and the errors in the zero-level offsets of the two maps introduced in Sect. 3. These errors are assumed, in a conservative way, to be equal to the corresponding rms values (0.75 MJy/sr and 0.09 MJy/sr at 1.15 mm and 2 mm, respectively). The  $\beta$  radial profiles are limited to an angular radius of  $40''$  in order to only use data with a signal-to-noise ratio above 10 in both NIKA bands (see Sect. 4).

In this diagram the different trends between the protostellar cores and the prestellar core are remarkable and listed in Table 2. The prestellar core has a flat profile while both protostellar cores reveal an increasing trend of  $\beta$  with radius, with  $\beta$  values that become consistent with those of the prestellar core at the farthest distance from the center. This effect is observed both when  $T_d(r)$  is obtained from the Abel inversion technique (coloured data points) and when it is deduced from the line-of-sight dust temperature (dashed lines). The mapmaking procedure applied to the NIKA data may affect the ratio map and the value of  $\beta$ . We thus repeated our analysis with the four different versions of the maps (see Sect. 3) and we show the corresponding  $\beta$  radial profiles with grey data points in the right panel of Fig. 5. Systematic effects related to the mapmaking do not significantly change our results. The different trends observed in the  $\beta$  profiles of the three sources are indeed preserved, although the total uncertainty in the absolute values increases. The  $\beta$  profile of the prestellar core is consistent with a constant value of  $\beta = 2.4 \pm 0.3$ .

Object	Slope (m) [arcsec <sup>-1</sup> ]	Inner $\beta$ value ( $\beta_{\text{in}}$ )
Miz-8b	$0.00 \pm 0.01$	$2.4 \pm 0.3$
K04166	$0.019 \pm 0.009$	$0.8 \pm 0.2$
K04169	$0.018 \pm 0.008$	$1.3 \pm 0.2$

**Table 2.** Parameters of the linear fit,  $\beta(r) = m \times r + \beta_{\text{in}}$ , to the  $\beta$  profiles shown in the right panel of Fig. 5, where  $r$  is the angular radius.

## 6. Discussion

In this section we discuss potential astrophysical biases affecting our results and provide plausible explanations of the  $\beta$  radial profiles shown in Fig. 5.

First of all, we notice that other types of radio emission, such as free-free or (gyro-)synchrotron radiation, are negligible compared to dust emission in this work. The Taurus molecular cloud is a low-mass star-forming region, differing from those studied in similar works such as Orion in Schnee et al. (2014) and in Sadavoy et al. (2016), with very few internal ionizing sources. Furthermore, all of the young stellar objects (YSOs) present in the field of Fig. 1 are low-luminosity objects ( $L_{\text{bol}} < 1 L_{\odot}$ ). Strong (gyro-)synchrotron emission is quite rare among such YSOs and restricted to Class-III objects (cf. André 1996). The base of the jets/outflows emanating from Class-0 (or -I) protostars produce weak free-free emission from shock-ionized gas in the centimeter range (Anglada 1996), but the expected contri-

<sup>4</sup>The standard deviation in  $R_{1,2}$  is obtained by propagating the errors in the mean values of  $I_{1\text{mm}}$  and  $I_{2\text{mm}}$  within bins of the radial distance.

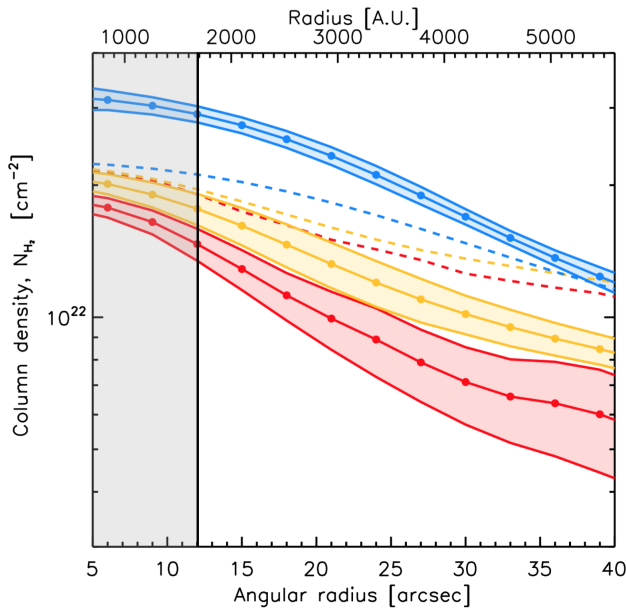


**Fig. 6.** Radial  $N_{H_2}$  column density profiles for K04166 (red), K04169 (yellow), and Miz-8b (blue), as derived from *Herschel* Gould Belt survey data. The colour-code is the same as in Fig. 5 as well as the grey-shaded area.

bution is negligible at mm wavelengths. The total free-free radio continuum flux scales with the outflow momentum rate and can be estimated from Eq. (1) of Anglada (1996) at 5 GHz. Given the outflow momentum rates measured by Bontemps et al. (1996) for the protostars K04166 and K04169, the expected free-free flux density is  $\sim 0.2$  mJy at 5 GHz, which scales to an upper limit of about  $\sim 0.6$  mJy at 150 GHz using a power-law frequency dependence with a spectral index of 0.3 for extrapolation (see Table 1 of Anglada 1996, for L1551-IRS5 in Taurus). Considering the NIKA rms noise level of  $\sim 1$  mJy/18.2''-beam at 150 GHz, we conclude that free-free radio contamination can definitely be neglected in our study, even for the protostellar cores. Shocked material associated with the outflows from the two protostars, K04166 and K04169 (Bontemps et al. 1996; Tafalla et al. 2010), may also have an unusually high dust emissivity index ( $\beta \sim 3$ ) (Gueth et al. 2003). However, we do not see evidence of such  $\beta$  values here.

We also made sure that CO contamination to the mm continuum is not significant for the three sources. In Fig. 2 we show that the only emitting transition that may be relevant for our study is the CO(2-1), which falls within NIKA band-1. However, using available FCRAO 12CO data (Narayanan et al. 2008), and integrating the line over the NIKA bandpass, we estimated that the total CO contamination is less than 1% of the NIKA surface brightness in the case of the two protostellar cores and even lower in the case of the prestellar core Miz-8b.

We also verified the hypothesis of optically thin dust emission in both band-1 and band-2. Given the Abel-reconstructed  $N_{H_2}$  radial profiles (see Fig. 6), obtained from the *Herschel* data by normalizing the greybody fit described in Sect. 5.2, and given Eq. 6, we can provide a rough estimate of the optical depth at 1.15 mm for the three objects as follows

$$\tau_{1\text{mm}} = \kappa_{1\text{mm}} \mu_{H_2} m_H N_{H_2}, \quad (8)$$

where  $\mu_{H_2} = 2.8$  (Kauffmann et al. 2008). Using the radial profiles in Fig. 6 the largest value of  $\tau_{1\text{mm}}$  on a 24''-scale obtained

for the prestellar core Miz-8b is 0.001, which is much smaller than unity. If instead of using  $\beta = 2$  in Eq. 6 we vary  $\beta$  between 1 and 3, results do not change.

In spite of the approximations made above, these estimates suggest that the trends seen in the  $\beta$  radial profiles of the three sources must be real and associated to changes in dust properties.

### 6.1. Astrophysical interpretation

A number of works already showed that dust-grain growth, up to mm-size, may cause lower values of dust emissivity indices (as low as 0) especially toward Class-II objects with protoplanetary disks (e.g. Guilloteau et al. 2011). Younger Class 0 objects in the Orion molecular cloud were also found with low  $\beta$  values ( $\sim 0.9$ ) compared to those of the diffuse ISM (Schnee et al. 2014), although a recent work by Sadavoy et al. (2016) revisited this result finding larger values between 1.7 and 1.8, reporting a lack of evidence for grain growth in OMC2/3. In this context our results represent an important contribution to the study of dust evolution at early stages of star formation. We may potentially be witnessing a change in the size distribution of dust grains going from the outer parts of protostellar cores, where  $\beta$  is compatible with that of the prestellar core Miz-8b, to the inner part, where the increase in dust-grain size and change in chemical composition (i.e. aliphatic-rich to aromatic-rich amorphous hydrocarbons, Jones et al. (2013)) may explain a larger emissivity of the grains, coupled with the drop of the  $\beta$  radial profiles toward the center. In addition to changes in  $\beta$ , we notice that intrinsic changes in  $\kappa_0$  (see Eq. 2), caused by grain growth, may also exist (Kramer et al. 2003). However, this effect cannot be constrained with NIKA data only, since the ratio  $R_{1,2}$  is independent of  $\kappa_0$  variations.

Another interpretation might explain our results. Both from theoretical models and laboratory experiments, it has been known for a while that because of the microphysics of dust grains the dust emissivity index in the mm range can depend on temperature: the higher the dust temperature the lower the  $\beta$  (Agladze et al. 1996; Mennella et al. 1998; Boudet et al. 2005; Meny et al. 2007; Coupeaud et al. 2011). In Fig. 7 we show the  $\beta$ - $T_d$  diagram relative to the three sources under study with the Abel-reconstructed dust temperature profiles. We also display the peak  $\beta$  values as a function of the Abel-reconstructed  $T_d$  for the prestellar cores Miz-2 and HGBS-1 (blue stars in Fig. 7). Overall, a clear anticorrelation between the two parameters is observed. Previous observational works performing dust SED fits with PRONAOS, ARCHEOPS, *Herschel*, and *Planck* data reported such an anticorrelation across different physical scales and astrophysical environments (e.g. Dupac et al. 2003; Désert et al. 2008; Bracco et al. 2011; Planck Collaboration XI 2014). While in most of these studies a possible statistical bias due to low signal-to-noise regions in the maps may mimic the intrinsic anticorrelation between  $\beta$  and  $T_d$  (Shetty et al. 2009), in the present work the observed trend is not sensitive to this effect. Indeed, we separately estimated the two parameters,  $\beta$  and  $T_d$ , based on NIKA and *Herschel* data respectively, without introducing any statistical correlation caused by noise. Nevertheless, as discussed in Coupeaud et al. (2011), because of many assumptions in the modelling (i.e., main focus on the disorder of the amorphous state of silicates), and of various spurious effects in observations (i.e., line-of-sight integration, noise), a one-to-one comparison between our results and theoretical expectations is complicated. Most laboratory experiments find an anticorrelation between  $\beta$  and  $T_d$  over a wide range in temperature ( $\sim 100$ K, Coupeaud et al. (2011)). Agladze et al. (1996)



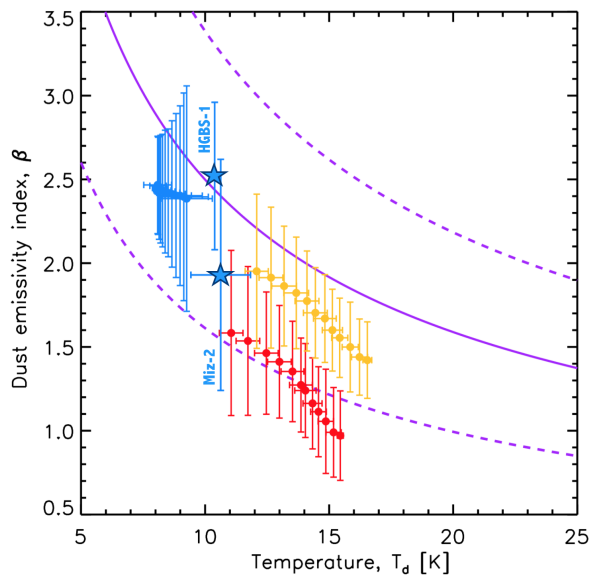


**Fig. 7.** Diagram of  $\beta$  against  $T_d$  for K04166 (red), K04169 (yellow), and Miz-8b (blue). For indication, the peak values for Miz-2 and HGBS-1 are also displayed with blue stars. The purple lines represent the empirical law (see Sect. 6) found in Désert et al. (2008) (solid line) and the corresponding  $1\text{-}\sigma$  uncertainty (dashed lines).

show the dependence between the two parameters in a range more similar to ours, with values of  $\beta$  close to 2.5 at 10K for *forsterite* and *enstatite* silicate grains and a shallower decrease of  $\beta$  with  $T_d$  at higher temperatures compared to our finding. Interestingly, the results displayed in Fig. 7 are in agreement (within  $1\sigma$ ) with the empirical power law of the form  $\beta(T_d) = (11.5 \pm 3.8)T_d^{(-0.660 \pm 0.054)}$  (purple in the figure), found by Désert et al. (2008) studying dust properties toward cold clumps in the Galactic plane with ARCHEOPS data.

We conclude that intrinsic changes in dust emissivity related to temperature variations may also play a role in the  $\beta$  radial profiles shown in Fig. 5, although a definite interpretation based on state-of-the-art dust models and laboratory data is yet to be achieved. We believe that the most likely scenario causing the decrease of  $\beta$  toward the center of protostellar cores is a combination of both grain growth and dust temperature effects.

## 7. Summary & prospects

Making use of the dual-band capability of NIKA to simultaneously observe the sky at 1.15 mm and 2 mm, in this paper we presented new results on the analysis of dust emissivity changes in the B213 filament of the Taurus molecular cloud (at a distance of  $\sim 140$ pc). The observed region is a  $8' \times 5'$  portion of a self-gravitating filament in the process of gravitational contraction toward its longest axis. The sub-parsec segment we focused on is of great interest since it presents a variety of early-type objects of star formation that very likely originated from the same parent filament. We showed a rare example of changes of dust properties correlated with the evolutionary stage of star formation.

By means of the ratio map of the two NIKA bands we showed that, in the Rayleigh-Jeans limit, the dust emissivity spectral index progressively decreases from prestellar cores ( $\beta_{RJ} \sim 2$ ) to protostellar cores ( $\beta_{RJ} \sim 1$ ) to a Class-II T-Tauri star

( $\beta_{RJ} \sim 0$ ). Using temperature radial profiles deduced from the *Herschel* data,  $T_d$ , we also presented radial profiles of the dust emissivity index,  $\beta$ , for two protostellar cores and one prestellar core, which were corrected for possible line-of-sight temperature gradients through the Abel transform inversion technique.

Our results showed that while a constant  $\beta$  profile of about  $2.4 \pm 0.3$  characterizes the prestellar core, decreasing  $\beta$  profiles toward the center are found for the two protostellar cores, reaching central values between  $\sim 1$  and  $\sim 1.5$ . A clear anticorrelation between  $\beta$  and  $T_d$  is also observed, which is consistent with previous observational works despite the lack of a theoretical framework able to accurately model it. We concluded that the observed changes in  $\beta$  with radius trace dust evolution from the prestellar to the protostellar stage, likely due to both grain-growth and dust temperature effects in the mm range.

In order to confirm this conclusion similar data should be acquired. Now the advent of the NIKA2 instrument on the IRAM-30m telescope (Calvo et al. 2016) will give us the chance to enlarge the observed sample of objects at early stages of star formation and characterize their physical properties at long wavelengths. Thanks to its polarization-sensitive capability at 1.2 mm (see Ritacco et al. 2017), the NIKA2 camera will also allow us to gain insight into the magnetic field structure of star-forming regions, especially at the scales where filaments fragment into prestellar cores, providing the community with an exceptional opportunity to enlighten one of the most important but yet poorly explored aspects of the star formation process.

*Acknowledgements.* We would like to thank the IRAM staff for their support during the campaigns. The NIKA dilution cryostat has been designed and built at the Institut Néel. In particular, we acknowledge the crucial contribution of the Cryogenics Group, and in particular Gregory Garde, Henri Rodenas, Jean Paul Leggeri, Philippe Camus. This work has been partially funded by the Foundation Nanoscience Grenoble, the LabEx FOCUS ANR-11-LABX-0013 and the ANR under the contracts 'MKIDS', 'NIKA', and 'NIKA2SKY' (ANR-15-CE31-0017). This work has benefited from the support of the European Research Council Advanced Grant ORISTARS under the European Union's Seventh Framework Programme (Grant Agreement no. 291294). We acknowledge fundings from the ENIGMASS French LabEx (R. A. and F. R.), the CNES post-doctoral fellowship program (R. A.), the CNES doctoral fellowship program (A. R.) and the FOCUS French LabEx doctoral fellowship program (A. R.). This research has made also use of data from the *Herschel* Gould Belt survey (HGBS) project (<http://gouldbelt-herschel.cea.fr>). The HGBS is a *Herschel* Key Programme jointly carried out by SPIRE Specialist Astronomy Group 3 (SAG 3), scientists of several institutes in the PACS Consortium (CEA Saclay, INAF-IFSI Rome and INAF-Arcetri, KU Leuven, MPIA Heidelberg), and scientists of the Herschel Science Center (HSC). P. P. acknowledges support from the Fundação para a Ciência e a Tecnologia of Portugal (FCT) through national funds (UID/FIS/04434/2013) and by FEDER through COMPETE2020 (POCI-01-0145-FEDER-007672) and also by the fellowship SFRH/BPD/110176/2015 funded by FCT (Portugal) and POPH/FSE (EC).

## References

- Adam, R., Bartalucci, I., Pratt, G. W., et al. 2017, *A&A*, 598, A115
- Adam, R., Comis, B., Macías-Pérez, J.-F., et al. 2015, *A&A*, 576, A12
- Adam, R., Comis, B., Macías-Pérez, J. F., et al. 2014, *A&A*, 569, A66
- Agladze, N. I., Sievers, A. J., Jones, S. A., Burlitch, J. M., & Beckwith, S. V. W. 1996, *ApJ*, 462, 1026
- André, P. 1996, in *Astronomical Society of the Pacific Conference Series*, Vol. 93, *Radio Emission from the Stars and the Sun*, ed. A. R. Taylor & J. M. Paredes, 273–284
- André, P., Di Francesco, J., Ward-Thompson, D., et al. 2014, *Protostars and Planets VI*, 27
- André, P., Men'shchikov, A., Bontemps, S., et al. 2010, *A&A*, 518, L102
- André, P., Ward-Thompson, D., & Barsony, M. 1993, *ApJ*, 406, 122
- André, P., Ward-Thompson, D., & Barsony, M. 2000, *Protostars and Planets IV*, 59
- Anglada, G. 1996, in *Astronomical Society of the Pacific Conference Series*, Vol. 93, *Radio Emission from the Stars and the Sun*, ed. A. R. Taylor & J. M. Paredes, 3–14

- Bontemps, S., André, P., Terebey, S., & Cabrit, S. 1996, *A&A*, 311, 858
- Boudet, N., Mutschke, H., Nayral, C., et al. 2005, *ApJ*, 633, 272
- Boulanger, F., Abergel, A., Bernard, J.-P., et al. 1996, *A&A*, 312, 256
- Bracco, A., Cooray, A., Veneziani, M., et al. 2011, *MNRAS*, 412, 1151
- Calvo, M., Benoît, A., Catalano, A., et al. 2016, *Journal of Low Temperature Physics*, 184, 816
- Calvo, M., Roesch, M., Désert, F.-X., et al. 2013, *A&A*, 551, L12
- Catalano, A., Calvo, M., Ponthieu, N., et al. 2014, *A&A*, 569, A9
- Compiègne, M., Verstraete, L., Jones, A., et al. 2011, *A&A*, 525, A103
- Coupeaud, A., Demyk, K., Meny, C., et al. 2011, *A&A*, 535, A124
- Davis, C. J., Chrysostomou, A., Hatchell, J., et al. 2010, *MNRAS*, 405, 759
- Désert, F.-X., Macías-Pérez, J. F., Mayet, F., et al. 2008, *A&A*, 481, 411
- Draine, B. T. 2006, *ApJ*, 636, 1114
- Draine, B. T. & Li, A. 2007, *ApJ*, 657, 810
- Dupac, X., Bernard, J.-P., Boudet, N., et al. 2003, *A&A*, 404, L11
- Elias, J. H. 1978, *ApJ*, 224, 857
- Furlan, E., McClure, M., Calvet, N., et al. 2008, *ApJS*, 176, 184
- Greene, T. P., Wilking, B. A., Andre, P., Young, E. T., & Lada, C. J. 1994, *ApJ*, 434, 614
- Gueth, F., Bachiller, R., & Tafalla, M. 2003, *A&A*, 401, L5
- Guilloteau, S., Dutrey, A., Piétu, V., & Boehler, Y. 2011, *A&A*, 529, A105
- Hacar, A., Tafalla, M., Kauffmann, J., & Kovács, A. 2013, *A&A*, 554, A55
- Hartmann, L. 2002, *ApJ*, 578, 914
- Hildebrand, R. H. 1983, *QJRAS*, 24, 267
- Hill, T., Motte, F., Didelon, P., et al. 2011, *A&A*, 533, A94
- Jones, A. P., Fanciullo, L., Köhler, M., et al. 2013, *A&A*, 558, A62
- Jones, A. P., Köhler, M., Ysard, N., Bocchio, M., & Verstraete, L. 2017, *ArXiv e-prints*
- Kauffmann, J., Bertoldi, F., Bourke, T. L., Evans, II, N. J., & Lee, C. W. 2008, *A&A*, 487, 993
- Kenyon, S. J., Calvet, N., & Hartmann, L. 1993, *ApJ*, 414, 676
- Kenyon, S. J., Hartmann, L. W., Strom, K. M., & Strom, S. E. 1990, *AJ*, 99, 869
- Könyves, V., André, P., Men'shchikov, A., et al. 2015, *A&A*, 584, A91
- Kramer, C., Richer, J., Mookerjee, B., Alves, J., & Lada, C. 2003, *A&A*, 399, 1073
- Lada, C. J. 1987, in *IAU Symposium*, Vol. 115, *Star Forming Regions*, ed. M. Peimbert & J. Jugaku, 1–17
- Lagache, G., Abergel, A., Boulanger, F., & Puget, J.-L. 1998, *A&A*, 333, 709
- Li, D. & Goldsmith, P. F. 2012, *ApJ*, 756, 12
- Malinen, J., Juvela, M., Collins, D. C., Lunttila, T., & Padoan, P. 2011, *A&A*, 530, A101
- Marsh, K. A., Kirk, J. M., André, P., et al. 2016, *MNRAS*, 459, 342
- Mathis, J. S., Rumpl, W., & Nordsieck, K. H. 1977, *ApJ*, 217, 425
- Mennella, V., Brucato, J. R., Colangeli, L., et al. 1998, *ApJ*, 496, 1058
- Men'shchikov, A., André, P., Didelon, P., et al. 2010, *A&A*, 518, L103
- Meny, C., Gromov, V., Boudet, N., et al. 2007, *A&A*, 468, 171
- Mizuno, A., Onishi, T., Hayashi, M., et al. 1994, *Nature*, 368, 719
- Molinari, S., Swinyard, B., Bally, J., et al. 2010, *PASP*, 122, 314
- Monfardini, A., Benoit, A., Bideaud, A., et al. 2011, *ApJS*, 194, 24
- Motte, F. & André, P. 2001, *A&A*, 365, 440
- Narayanan, G., Heyer, M. H., Brunt, C., et al. 2008, *ApJS*, 177, 341
- Onishi, T., Mizuno, A., Kawamura, A., Tachihara, K., & Fukui, Y. 2002, *ApJ*, 575, 950
- Palmeirim, P., André, P., Kirk, J., et al. 2013, *A&A*, 550, A38
- Paradis, D., Veneziani, M., Noriega-Crespo, A., et al. 2010, *A&A*, 520, L8
- Planck Collaboration XI. 2014, *A&A*, 571, A11
- Ritacco, A., Ponthieu, N., Catalano, A., et al. 2017, *A&A*, 599, A34
- Roy, A., André, P., Palmeirim, P., et al. 2014, *A&A*, 562, A138
- Sadavoy, S. I., Di Francesco, J., Johnstone, D., et al. 2013, *ApJ*, 767, 126
- Sadavoy, S. I., Stutz, A. M., Schnee, S., et al. 2016, *A&A*, 588, A30
- Santiago-García, J., Tafalla, M., Johnstone, D., & Bachiller, R. 2009, *A&A*, 495, 169
- Schmalzl, M., Kainulainen, J., Quanz, S. P., et al. 2010, *ApJ*, 725, 1327
- Schnee, S., Mason, B., Di Francesco, J., et al. 2014, *MNRAS*, 444, 2303
- Schneider, S. & Elmegreen, B. G. 1979, *ApJS*, 41, 87
- Shetty, R., Kauffmann, J., Schnee, S., & Goodman, A. A. 2009, *ApJ*, 696, 676
- Stepnik, B., Abergel, A., Bernard, J.-P., et al. 2003, *A&A*, 398, 551
- Tafalla, M., Santiago, J., Johnstone, D., & Bachiller, R. 2004, *A&A*, 423, L21
- Tafalla, M., Santiago-García, J., Hacar, A., & Bachiller, R. 2010, *A&A*, 522, A91
- Tatematsu, K., Umemoto, T., Kandori, R., & Sekimoto, Y. 2004, *ApJ*, 606, 333
- Testi, L., Birnstiel, T., Ricci, L., et al. 2014, *Protostars and Planets VI*, 339
- Weingartner, J. C. & Draine, B. T. 2001, *ApJ*, 553, 581
- Ysard, N., Abergel, A., Ristorcelli, I., et al. 2013, *A&A*, 559, A133
- Ysard, N., Köhler, M., Jones, A., et al. 2015, *A&A*, 577, A110

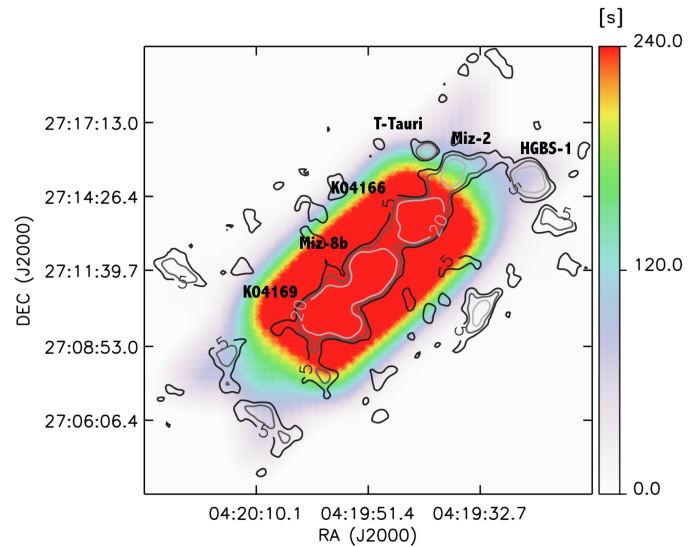


**Fig. A.1.** Time-per-pixel map with contours of the 1.15 mm brightness as in the left panel of Fig. 1.

## Appendix A: Time coverage of the NIKA maps

In this Appendix we show the time-per-pixel map that corresponds to the NIKA observations presented in the paper. In Fig. A.1 the time-per-pixel is shown in units of seconds with the 1.15 mm brightness in contours as in the left panel of Fig. 1. We use this map to justify our choice to detail the analysis of dust properties only for the three sources that were longer observed (i.e. K04166, K04169, and Miz-8b). These objects are also those lying at the center of the field of view, where systematic effects due to the scanning strategy are less significant.